Measurement of the neutrino neutral-current elastic differential cross section on mineral oil at $E_\nu \sim 1$ GeV

A. A. Aguilar-Arevalo,[14] C. E. Anderson,[19] A. O. Bazarko,[16] S. J. Brice,[8] B. C. Brown,[8] L. Bugel,[12] J. Cao,[14] L. Coney,[5] J. M. Conrad,[13] D. C. Cox,[10] A. Curioni,[19] R. Dharmapalan,[1] Z. Djurcic,[2] D. A. Finley,[8] B. T. Fleming,[19] R. Ford,[8] F. G. Garcia,[8] G. T. Garvey,[11] J. Grange,[9] C. Green,[8,11] J. A. Green,[10,11] T. L. Hart,[5] E. Hawker,[4,11] R. Imlay,[12] R. A. Johnson,[4] G. Karagiorgi,[13] P. Kasper,[8] T. Katori,[10,13] T. Kobilarcik,[8] I. Kourbanis,[8] S. Koutsoliotas,[3] E. M. Laird,[16] S. K. Linden,[19] J. M. Link,[18] Y. Liu,[15] Y. Liu,[1] W. C. Louis,[11] K. B. M. Mahn,[6] W. Marsh,[8] C. Mauger,[11] V. T. McGary,[13] G. McGregor,[11] W. Metcalf,[12] P. D. Meyers,[16] F. Mills,[8] G. B. Mills,[11] J. Monroe,[6] C. D. Moore,[8] J. Mousseau,[9] R. H. Nelson,[5] P. Nienaber,[17] J. A. Nowak,[12] B. Osmanov,[9] S. Ouedraogo,[12] R. B. Patterson,[16] Z. Pavlovic,[11] D. Perevalov,[1,8] C. C. Polly,[8] E. Prebys,[8] J. L. Raaf,[4] H. Ray,[9] B. P. Roe,[15] A. D. Russell,[8] V. Sandberg,[11] R. Schirato,[11] D. Schmitz,[8] M. H. Shaevitz,[6] F. C. Shoemaker,[16,*] D. Smith,[7] M. Soderberg,[19] M. Sorel,[6,†] P. Spentzouris,[8] J. Spitz,[19] I. Stancu,[1] R. J. Stefanski,[8] M. Sung,[12] H. A. Tanaka,[16] R. Tayloe,[10] M. Tzanov,[5] R. G. Van de Water,[11] M. O. Wascko,[12,‡] D. H. White,[11] M. J. Wilking,[5] H. J. Yang,[15] G. P. Zeller,[8] and E. D. Zimmerman[5]

(MiniBooNE Collaboration)

[1]*University of Alabama, Tuscaloosa, Alabama 35487, USA*
[2]*Argonne National Laboratory, Argonne, Illinois 60439, USA*
[3]*Bucknell University, Lewisburg, Pennsylvania 17837, USA*
[4]*University of Cincinnati, Cincinnati, Ohio 45221, USA*
[5]*University of Colorado, Boulder, Colorado 80309, USA*
[6]*Columbia University, New York, New York 10027, USA*
[7]*Embry Riddle Aeronautical University, Prescott, Arizona 86301, USA*
[8]*Fermi National Accelerator Laboratory, Batavia, Illinois 60510, USA*
[9]*University of Florida, Gainesville, Florida 32611, USA*
[10]*Indiana University, Bloomington, Indiana 47405, USA*
[11]*Los Alamos National Laboratory, Los Alamos, New Mexico 87545, USA*
[12]*Louisiana State University, Baton Rouge, Louisiana 70803, USA*
[13]*Massachusetts Institute of Technology, Cambridge, Massachusetts 02139, USA*
[14]*Instituto de Ciencias Nucleares, Universidad National Autónoma de México, D.F. 04510, México*
[15]*University of Michigan, Ann Arbor, Michigan 48109, USA*
[16]*Princeton University, Princeton, New Jersey 08544, USA*
[17]*Saint Mary's University of Minnesota, Winona, Minnesota 55987, USA*
[18]*Virginia Polytechnic Institute and State University, Blacksburg, Virginia 24061, USA*
[19]*Yale University, New Haven, Connecticut 06520, USA*

We report a measurement of the flux-averaged neutral-current elastic differential cross section for neutrinos scattering on mineral oil (CH_2) as a function of four-momentum transferred squared, Q^2. It is obtained by measuring the kinematics of recoiling nucleons with kinetic energy greater than 50 MeV which are readily detected in MiniBooNE. This differential cross-section distribution is fit with fixed nucleon form factors apart from an axial mass M_A that provides a best fit for $M_A = 1.39 \pm 0.11$ GeV. Using the data from the charged-current neutrino interaction sample, a ratio of neutral-current to charged-current quasielastic cross sections as a function of Q^2 has been measured. Additionally, single protons with kinetic energies above 350 MeV can be distinguished from neutrons and multiple nucleon events. Using this marker, the strange quark contribution to the neutral-current axial vector form factor at $Q^2 = 0$, Δs, is found to be $\Delta s = 0.08 \pm 0.26$.

---

*Deceased.
†Present address: IFIC, Universidad de Valencia and CSIC, Valencia 46071, Spain.
‡Present address: Imperial College, London SW7 2AZ, United Kingdom.

I. INTRODUCTION

Neutrino-nucleon neutral-current elastic (NCE) scattering is a unique and fundamental probe of the nucleon. NCE scattering on a nuclear target such as carbon may be viewed as scattering from the individual nucleons but may also include contributions from collective nuclear effects. This process should be sensitive to nucleon isoscalar weak currents as opposed to charged-current quasielastic (CCQE) scattering which interacts only via isovector weak currents. Therefore, the NCE process can be used to search for strange quarks in the nucleon which may show themselves via the isoscalar weak current. In addition, the NCE process offers a complementary channel to CCQE to investigate any substantial collective nuclear effects in a nucleus such as carbon.

Over the years, a handful of experiments have measured (anti)neutrino-proton neutral-current elastic scattering cross sections, most commonly as ratios to QE scattering [1–7]. The most recent and highest statistics measurement was conducted in the mid-1980s at Brookhaven National Laboratory (BNL) using a 170 ton liquid scintillator detector operating in a horn-focused neutrino (antineutrino) beam. In this case, BNL E734 recorded 1686 $\nu p \rightarrow \nu p$ and 1821 $\bar{\nu} p \rightarrow \bar{\nu} p$ candidate events allowing for measurements of the differential cross section for this process as a function of four-momentum transfer squared (Q^2). These were effectively NCE/CCQE differential cross-section ratios as the BNL neutrino flux was determined from a CCQE event sample [8].

The MiniBooNE experiment [9,10], while designed to search for neutrino oscillations, also has the capability to measure NCE scattering given that NCE events account for about 18% of the total neutrino sample collected. A large fraction of these neutral-current events are readily observable in the MiniBooNE detector which uses pure mineral oil (CH_2) as a detector medium. The detector is predominantly a Cherenkov detector, however, fluors presented in the mineral oil produce a small amount of scintillation light well below Cherenkov threshold for relativistic charged particles (such as electrons, muons, protons, etc.). The absence of prompt Cherenkov light allows for the identification and measurement of the recoiling nucleons produced in neutrino NCE scattering.

The main result presented in this paper is a high-statistics measurement of the flux-averaged differential cross section as a function of Q^2 for NCE scattering on CH_2 in MiniBooNE for 0.1 GeV^2 < Q^2 < 1.65 GeV^2. It is presented as scattering from individual nucleons both bound (in carbon) and free (in hydrogen). However, it is acknowledged that nuclear effects may well be important for full understanding of this data.

A preliminary measurement of the MiniBooNE NCE differential cross section had been performed early on using 6.57×10^{19} protons on the neutrino production target (POT) [11]. The results presented in this paper are based on the entire data set in neutrino mode, for a total of 6.46×10^{20} POT and an improved event reconstruction. MiniBooNE has also collected antineutrino data which will be presented in subsequent works.

To characterize the NCE from carbon in MiniBooNE, the relativistic Fermi gas model of Smith and Moniz is used as described in Sec. II D. Within this model, two fundamental parameters are employed: the nucleon axial mass M_A and the strange quark contribution to the axial form factor, Δs. It is acknowledged that nuclear effects in carbon may cause this axial mass to be an ''effective'' value and not the same as that for scattering from free nucleons. The formalism for NCE scattering on free nucleons, which is basic to any model-dependent approach to characterize the NCE data, is summarized in Appendix B.

While the generally accepted value for M_A is 1.026 ± 0.021 GeV [12], recent experiments [13–16] measuring CCQE from nuclear targets have found it useful to employ values that are 20%–30% larger to fit the Q^2 dependence of their observed yields. It may be that this increased value of M_A should be understood not as the M_A obtained for free nucleons but rather as a parametrization of neglected nuclear effects [17,18]. Regardless, an extraction of M_A from NCE scattering offers a complementary test to the M_A determined from CCQE.

Previously, BNL E734 is the only experiment to report an M_A measurement from a NCE sample. They obtain $M_A = 1.06 \pm 0.05$ GeV [7] fitting their measured $\nu p \rightarrow \nu p$ and $\bar{\nu} p \rightarrow \bar{\nu} p$ differential cross sections as a function of Q^2. A later reanalysis of that sample data obtained similarly small values of M_A [19]. In this paper, a measurement of M_A is determined from NCE scattering independent of CCQE.

The strange quark contribution to the nucleon spin at $Q^2 = 0$, Δs, can also be extracted via the NCE process within a relativistic Fermi gas model. The NCE differential cross section at low Q^2 is sensitive to Δs [20] for both neutrinos and antineutrinos. The BNL E734 experiment measured these processes and reported $\Delta s = -0.15 \pm 0.09$ [7,19,21]. However, ratio measurements offer the possibility for extracting Δs at low Q^2 with reduced systematic errors. For example, a measurement of $(\nu p \rightarrow \nu p)/(\nu_\mu n \rightarrow \mu p)$ has been proposed by the FINeSSE experiment [22]. In this paper, a ratio of $(\nu p \rightarrow \nu p)/(\nu N \rightarrow \nu N)$ at $Q^2 > 0.7$ GeV is used to extract Δs, where N is a neutron or proton.

In the following sections the MiniBooNE experiment is described, including a description of the neutrino beam line, detector, neutrino flux prediction, and the cross-section model used to predict the rates of different neutrino interactions in the detector. In Secs. III and IV, methods and techniques used in the NCE analysis are presented together with various results, including the NCE differential cross section, the NCE/CCQE ratio and measurements of M_A and Δs. Section V contains a summary of the paper.

Also, Appendixes A and B have additional information useful for interpreting the results which is not included in the main text.

II. MINIBOONE EXPERIMENT

A. Neutrino beam line

The Booster Neutrino Beam line (BNB) at the Fermi National Accelerator Laboratory uses a beam of protons with momentum 8.89 GeV/c to produce an intense and almost pure beam of ν_μ with an average energy of about 800 MeV. Protons are extracted from the Fermilab Booster in 1.6 μs pulses with $\sim 4 \times 10^{12}$ protons in each beam pulse. They are delivered onto a beryllium target, where a secondary beam of mesons is produced in p-Be interactions. Mesons are passed through a magnetic horn, a device which focuses positively charged particles and defocuses negatively charged particles. Mesons decay in an air-filled decay pipe producing a beam of neutrinos. Using the magnetic horn increases the neutrino flux at the MiniBooNE detector by a factor of ~ 6. The details on the BNB components can be found in Ref. [9].

B. Neutrino flux prediction

The neutrino flux at the detector is calculated via a GEANT4-based [23] Monte Carlo (MC) beam simulation. The simulation includes a full beam geometry, specified by shape, location, and material composition of the BNB components. The MC generates protons upstream of the target and propagates them through the target, generating and propagating products of p-Be interactions through the rest of the simulated BNB. In the ν_μ flux at the MiniBooNE detector, 96.7% of neutrinos are produced via $\pi^+ \rightarrow \mu^+ + \nu_\mu$ decay. The π^+ production double differential cross section used in the beam MC is based on a fit to an external measurement from the HARP

FIG. 1 (color online). Neutrino flux at the MiniBooNE detector for different types of neutrinos as a function of their energy as reported in [9,25].

experiment on the same target and with the same proton beam energy as in the BNB [24].

The neutrino flux prediction for different types of neutrino species is shown in Fig. 1. Flux tables are available in Ref. [25]. The π^+ production contribution to the neutrino flux uncertainty is about 5% at the peak of the flux distribution, increasing significantly at low and high neutrino energies. Other contributions to the flux error include uncertainties on other mesons production cross sections, the number of POT, and the horn magnetic field [9,26].

C. Detector

The MiniBooNE detector is situated 541 m from the Be target, under 3 m of overburden in order to reduce cosmic backgrounds. It is a 12.2 m diameter spherical steel tank, filled with mineral oil. The tank is divided into two optically isolated regions: a *signal* region being an inner sphere of radius 5.75 m and a *veto* region that is an outer shell with a thickness of 0.35 m. Photomultiplier tubes (PMTs) are used to detect photons emitted by the charged particles which are produced in the neutrino interactions. Charged particles may emit both Cherenkov and scintillation light. Information from all PMTs is used to identify and reconstruct the products of neutrino interactions.

A total of 1520 8-inch PMTs [27] are instrumented in the detector. There are 1280 PMTs attached to the spherical barrier from the inside, in the signal region, facing toward the center of the tank and distributed approximately uniformly. The remaining 240 PMTs are placed in the veto region and are used to tag charged particles entering or leaving the tank. The veto PMTs are mounted back-to-back, tangentially to the optical barrier, in order to have as much veto view as possible. Details on the MiniBooNE detector can be found elsewhere [10].

D. Cross-section model

Neutrino interactions within the detector are simulated with the NUANCE-V3 event generator [28], where the relativistic Fermi gas model of Smith and Moniz [29] is used to describe NCE scattering. Fermi momentum for carbon is taken to be 220 ± 20 MeV and binding energy 34 ± 9 MeV.

The contribution from strange quarks to the vector and axial vector form factors is taken to be zero. The error on Δs is taken to be 0.1. The value of M_A used in the MC is different for the quasielastic (both neutral and charged-current) scattering on carbon and hydrogen: For scattering on carbon $M_A = 1.230 \pm 0.077$ GeV is used (as measured from the CCQE channel in MiniBooNE [13]), while for scattering on hydrogen $M_A = 1.13 \pm 0.10$ GeV is used (which is the average between the values measured by the deuterium-based scattering experiments and MiniBooNE).

For resonant pion production, the Rein and Sehgal model [30] is used. In the few GeV range, such processes are
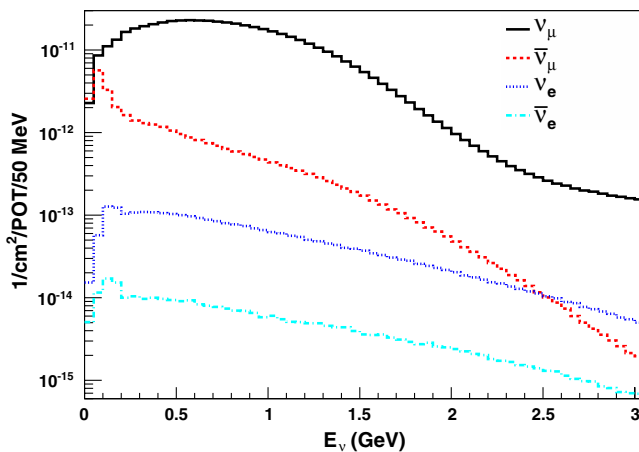
dominated by the $\Delta(1232)$ resonance, although contributions from higher mass resonances are also included in the MC. A value of $M_A^{1\pi} = 1.10 \pm 0.27$ GeV is used for both charge current (CC) and NC single pion events as determined from external data [31–34]. For multipion production processes, a value of $M_A^{N\pi} = 1.30 \pm 0.52$ GeV is assumed so that the sum of the exclusive CC channels reproduces CC inclusive data [35].

Intranuclear final state interactions (FSI) inside the carbon nucleus are modeled in NUANCE using a binary cascade model [28], where the scattered hadrons are propagated through the nucleus, which is simulated based on models of nuclear density and Fermi momentum. Because of FSI, a NCE interaction may produce more than one final state particle (other than the neutrino). For NCE scattering on carbon, the probability of producing multiple nucleons is $\sim 26\%$ integrated over the MiniBooNE flux, according to NUANCE. Also, a NC pion event might not contain any pions in the final state as the pion can be absorbed in the carbon nucleus or the baryonic resonance reinteracts without decaying. These are the dominant mechanisms by which NC pion events can become backgrounds to this analysis. The probability that a pion is absorbed is $\sim 20\%$ in carbon for MiniBooNE energies, according to the NUANCE simulation. The intranuclear pion absorption cross section is assigned a 25% uncertainty based on external pion-carbon data [36–38], and $\Delta N \rightarrow NN$ interactions are assigned a 100% uncertainty.

Neutrino interactions outside the detector, in the surrounding dirt or in the detector material (referred to as ''dirt'' background henceforth), are simulated the same way as the in-tank interactions but with a cross section reweighted according to the density of the material relative to that of the mineral oil.

Particle propagation in the detector is modeled using a GEANT3-based [39] MC with GCALOR [40] hadronic interactions simulating the detector response to particles produced in the neutrino interactions. GCALOR was chosen over GFLUKA [41] simulation, as it provides a better model of π^+ interactions on carbon [42].

III. NEUTRAL-CURRENT ELASTIC ANALYSIS

A. Event reconstruction

Event reconstruction in MiniBooNE is based on finding a set of parameters (position, time, direction, and energy—where applicable) which maximizes the event likelihood using the charge and time information from all PMTs. Each event is reconstructed using some combination of six different event hypotheses—single proton (NCE-like), single muon (ν_μ CCQE-like), single electron (ν_e CCQE-like), single π^0 (NC π^0 productionlike), muon and π^+ with the same vertex (ν_μ CC π^+ productionlike), and muon and π^0 with the same vertex (ν_μ CC π^0 production-like). A charge-time likelihood minimization method [43]

is used to obtain the best estimate of the kinematic observables in each event hypothesis. Under the NCE hypothesis, each event is assumed to be a pointlike proton with Cherenkov and scintillation light emission profiles determined from the MC. The output variables from these event reconstructions (such as likelihood ratios between two different event hypotheses) allow for particle identification.

The resulting position resolution is ~ 0.75 m for proton events in the detector and ~ 1.35 m for neutrons, with an energy resolution of $\sim 20\%$ for protons and $\sim 30\%$ for neutrons. For protons above Cherenkov threshold, the direction resolution is $\sim 10°$.

Light emission properties of protons differ from those of other charged particles in the detector, allowing for their particle identification. For instance, protons differ from electrons in terms of the fraction of prompt light emitted, defined as the fraction of PMT hits with a corrected time between -5 and 5 ns, as illustrated in Fig. 2, where the corrected time is the time difference between the PMT hit time and the reconstructed event time, with light propagation time from the reconstructed vertex to the PMT also taken into account.

Being neutral particles, neutrons themselves do not cause light emission in the detector. However we may detect them through their subsequent strong reinteractions, in which usually energetic protons are produced. Because we detect NCE neutrons only through secondary protons, they are virtually indistinguishable from NCE proton events.

For MiniBooNE NCE interactions, the total charge on all PMTs is proportional to the sum of kinetic energies of all final state nucleons that are produced in the interaction, which is referred to throughout this paper as T. It is important to understand that the nucleon kinetic energy measured this way is different from the one determined from the track-based reconstruction used in the SciBooNE
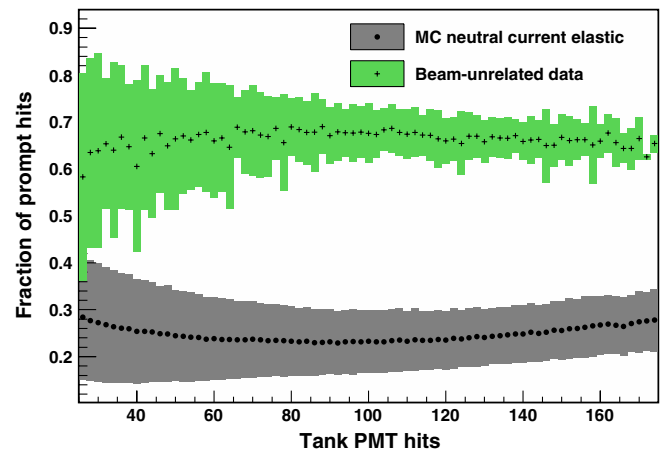

FIG. 2 (color online).   Fraction of prompt hits versus the total number of tank PMT hits for beam-unrelated data and NCE MC events reconstructed under an electron hypothesis. The error bars correspond to the root mean square of the distributions.

[44] and BNL E734 [7] experiments. In that case, the reconstructed proton track length is proportional to the kinetic energy of the most energetic proton produced in the event. Also the particle identification in MiniBooNE is based almost entirely on the properties of the measured Cherenkov ring (such as ring sharpness, charge, and time likelihoods), whereas the track-based experiments mostly use the particle's energy loss along the track.

B. Event selection

The following set of selection criteria (cuts) are applied to the full MiniBooNE data set to select the NCE sample:

(1) Only 1 *subevent* to ensure the event is NC and includes no decaying particles (e.g., μ decay). A subevent is a cluster of at least 10 tank PMT hits for which there is no more than 10 ns between any two consecutive hits. For example, a CCQE event typically contains two subevents; the first subevent is associated with the outgoing muon, while the second is associated with the subsequent decay electron [26].

(2) Number of veto PMT hits is less than 6 to remove events exiting or entering the detector: V hits < 6.

(3) Number of tank PMT hits is greater than 24 to ensure a reliable reconstruction: T hits > 24.

(4) Beam time window cut in order to consider only events time-coincident with the neutrino beam.

(5) Reconstructed proton energy of $T < 650$ MeV (above which the signal to background ratio decreases significantly).

(6) Log-likelihood ratio between electron and proton event hypotheses of $\ln(\mathcal{L}_e/\mathcal{L}_p) < 0.42$. The purpose of this cut is to eliminate beam-unrelated electrons from cosmic-ray muon decays. Even though

the variable shown in Fig. 2 provides a good separation between proton and electron events, it was found that the log-likelihood ratio is most effective in capturing all differences between the NCE signal and this background. The $\ln(\mathcal{L}_e/\mathcal{L}_p)$ variable and the value of the cut are shown in Fig. 3 for simulated NCE and the beam-unrelated data. The beam-unrelated data events are mostly muon decay (Michel) electrons.

(7) A fiducial volume cut, defined as follows:

$$R_{\text{fiducial}}(T) = \begin{cases} R < 4.2 \text{ m} & \text{if } T < 200 \text{ MeV}, \\ R < 5.0 \text{ m} & \text{if } T > 200 \text{ MeV}. \end{cases}$$

A tighter fiducial volume is required at low energies to reduce the dirt background.

A total of 94 531 events pass the NCE cuts resulting from 6.46×10^{20} POT. This is the largest NCE event sample collected to date. The efficiency of the cuts is estimated to be 35%, a large portion of which stems from the fiducial volume cut. We consider all NCE events with original vertices inside the detector as *signal*. The predicted fraction of NCE events in the sample is 65%. The remaining 35% of events are *backgrounds* of different types: 15% are NCE-like backgrounds, 10% dirt events, and 10% other backgrounds (of which only 0.5% are beam-unrelated). The reconstructed nucleon kinetic energy spectrum for selected NCE events with a uniform fiducial volume cut is shown in Fig. 4 along with the predicted background contributions.

The NCE-like background consists of NC pion production channels with no pion in the final state (i.e. the pion is absorbed in the initial target nucleus through FSI). In this case, the final state particles for these events are solely nucleons. In MiniBooNE, this is indistinguishable from the final state produced in NCE events and hence why these
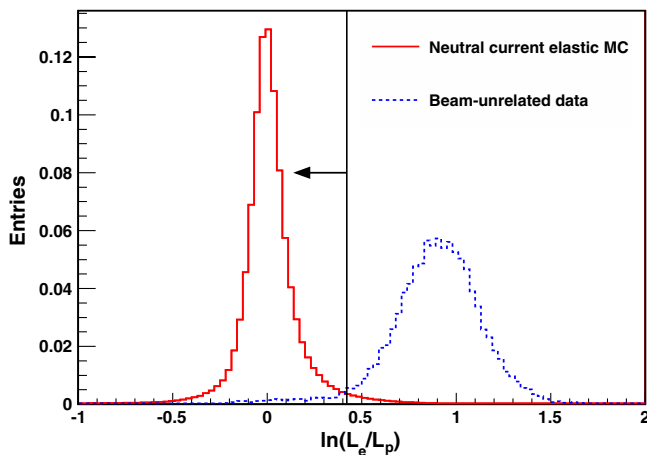

FIG. 3 (color online). Log-likelihood ratio between electron and proton event hypotheses for MC-generated NCE scattering events and beam-unrelated data. Both histograms are normalized to unit area. Events with $\ln(\mathcal{L}_e/\mathcal{L}_p) < 0.42$ are selected for the analysis.
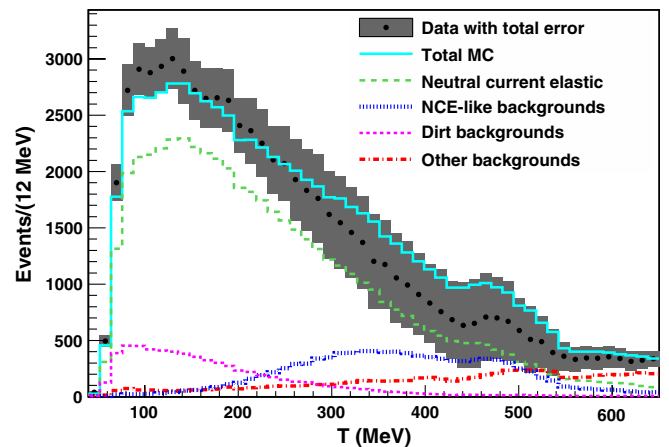

FIG. 4 (color online). Reconstructed nucleon kinetic energy spectra for the data and MC after the NCE event selection and a uniform fiducial volume cut of $R < 4.2$ m are applied. All MC distributions are normalized to the number of POT).

events are referred to as NCE-like background. The NCE-like background contributes mostly at intermediate energies 200 MeV $< T <$ 500 MeV.

The dirt background is an important contribution to the NCE data sample at low energies, most significantly below 200 MeV. This background is due to nucleons (mainly neutrons) which are produced in neutrino interactions outside of the detector, penetrating into the detector without firing enough veto PMTs. Dirt events are challenging to simulate in the MC because they occur in various media that have not been studied in detail (in the soil, detector support structures, etc.). However, we directly constrain this background using MiniBooNE data. Dirt events can be isolated from in-tank interactions using their distinct kinematics: Dirt events are preferentially reconstructed in the most upstream ($Z <$ 0 m) and outer regions of the detector with relatively low energies (small values of T). The dirt energy spectrum is measured by fitting dirt-enriched samples in the variables Z, R, and T, as explained in detail in Appendix A.

Other backgrounds are mainly charged-current channels but also include neutral-current pion production, beam-unrelated, and antineutrino NCE events. These backgrounds become relevant at high reconstructed energies, mainly above 400 MeV.

C. Unfolding

In order to obtain the cross section, we first subtract backgrounds that were constrained, namely, those beam-unrelated and dirt backgrounds. After this simple procedure the reconstructed energy spectrum for the data is multiplied by the signal fraction, which is the number of NCE events divided by the total number of neutrino induced in-tank events according to MC prediction, bin by bin. The obtained NCE reconstructed energy spectrum is then corrected for detector resolution and efficiency effects that distort the original spectrum. The correction is applied by unfolding the distribution using a method based on Bayes' theorem [45]. One can express the described unfolding procedure in the following equation [43]:

$$\sigma_i = \frac{\sum_j U_{ij}(d_j - D_j - V_j)\frac{S_j}{S_j + B_j}}{\epsilon_i \cdot (2m_N \Delta T) \cdot N_N \cdot N_{POT} \cdot \Phi}, \quad (1)$$

where the index j labels the reconstructed bin and i labels the unfolded (estimate of the true) bin. In this equation d represents data, S is predicted NCE events, D is measured dirt backgrounds, V is measured beam-unrelated backgrounds, B is the rest of the backgrounds (including NCE-like), ϵ is the efficiency, N_N is the number of nucleons in the detector, N_{POT} is the number of protons on target, ΔT is the bin width of the reconstructed energy distribution, and Φ is the neutrino flux (both ν_μ and ν_e), integrated for the E_ν range from 0 to 10 GeV. The unfolding matrix U is calculated for NCE events in the MC using a migration
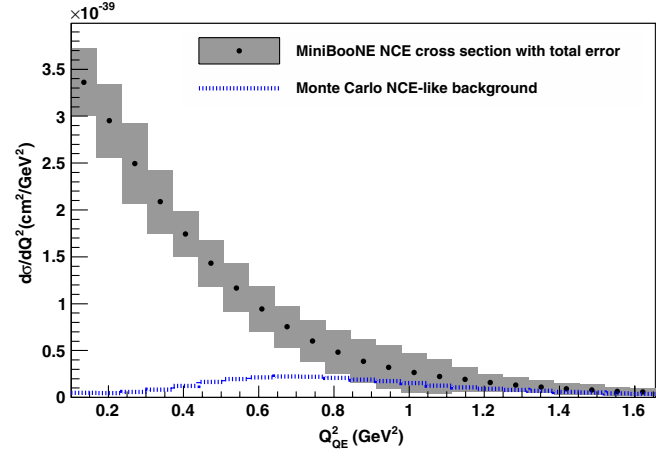

FIG. 5 (color online). The MiniBooNE NCE ($\nu N \rightarrow \nu N$) flux-averaged differential cross section on CH_2 as a function of $Q^2_{QE} = 2m_N\sum_i T_i$, where we sum the true kinetic energies of all final state nucleons produced in the NCE interaction. The blue dotted line is the predicted spectrum of NCE-like background which has been subtracted out from the total NCE-like differential cross section.

matrix of the true nucleon kinetic energy (the sum of the kinetic energies of all nucleons in the final state) versus the reconstructed nucleon kinetic energy.

This method gives a well-behaved but biased solution, which depends on the original MC energy spectrum. The error due to the unfolding bias is estimated by iterating the unfolding procedure for each MC variation, where the new MC energy spectrum is replaced by the unfolded energy spectrum. The details of the unfolding procedure used in the measurement and the error estimation associated with its bias can be found in Ref. [43]. The detector resolution and cut efficiency effects can be seen by comparing the reconstructed energy spectrum before unfolding (Fig. 4) and the final cross-section result (Fig. 5), which we shall discuss later.

D. Neutral-current elastic flux-averaged cross section

For each NCE event, Q^2 can be determined by measuring the total kinetic energy of outgoing nucleons in the interaction assuming the target nucleon is at rest. In this case we define

$$Q^2_{QE} = 2m_N T = 2m_N \sum_i T_i,$$

where m_N is the nucleon mass and T is the sum of the kinetic energies of the final state nucleons. MiniBooNE reports the NCE differential cross section as a function of this variable, Q^2_{QE}.

The MiniBooNE NCE differential cross section is less sensitive to FSI effects than those measured by tracking detectors, such as BNL E734 [7]. In case of a FSI, where no pions in the final state have been produced, the energy transferred by the neutrino may be divided among several

TABLE I.   Individual error contributions to the total integrated normalization uncertainty on the MiniBooNE measured NCE cross section. The statistical error of 2.5% is not included in the total normalization error.

Type of error	Error	Value (%)
Flux	Flux	6.7
Cross section	NC π^0 production yield	0.5
	In-tank background cross section	6.3
	Dirt background	1.0
Detector	Discriminator threshold	0.6
	Optical model	15.4
	Charge-time PMT response	2.1
	Hadronic interactions	0.5
Total		18.1

FIG. 6 (color online).   MiniBooNE NCE/CCQE cross section ratio on CH_2 as a function of Q^2_{QE}. The NUANCE MC prediction is plotted for two assumptions of parameters: the black solid line for $M_A = 1.23$ GeV and $\kappa = 1.022$ [13] and the blue dotted line for $M_A = 1.35$ GeV and $\kappa = 1.007$ [26]. Δs is assumed to be zero in both of these cases. Both cross sections in the ratio are per target nucleon—there are 14/6 times more target nucleons in the numerator than in the denominator. The error bars represent both statistical and all systematic uncertainties (excluding flux errors) taken in quadrature.

outgoing nucleons, but the total energy released in the MiniBooNE detector stays roughly the same due to energy conservation. Track-based detectors measure Q^2 by the proton track length and its angle with respect to the beam direction, which are kinematic observables of the most energetic proton produced in the NCE event. In that case, FSI may have large effects on the kinematics of individual outgoing nucleons, including the most energetic nucleon. Of course, there are still some FSI interactions producing final state pions which must be modeled and which can affect MiniBooNE NCE cross-section measurement.

The resulting NCE flux-averaged differential cross section on CH_2 is shown in Fig. 5 as a function of Q^2_{QE}. The predicted distribution of the NCE-like background, which has been subtracted along with the rest of backgrounds, is also shown in the figure. The NCE scattering is a sum of three different processes: scattering on free protons in hydrogen, bound protons in carbon, and bound neutrons in carbon. A detailed description of the contributions of each of these processes to the total MiniBooNE NCE cross section is given in Appendix B.

Systematic uncertainties and their contribution to the total error have been studied. The normalization error can be represented by a single number, shown in Table I. The largest systematic error in the NC analysis, the optical model, arises from the uncertainty on both Cherenkov and scintillation light production by charged particles in mineral oil. Cherenkov light production has been calibrated on cosmic muons, Michel electrons, and neutral pions [10]. An error of 20% on this amplitude of scintillation light generated by sub-Cherenkov particles in the detector has been assigned through a combination of benchtop measurements and *in situ* calibrations (see Appendix C of Ref. [43] for details).

E. Neutral-current elastic to charged-current quasielastic cross-section ratio measurement

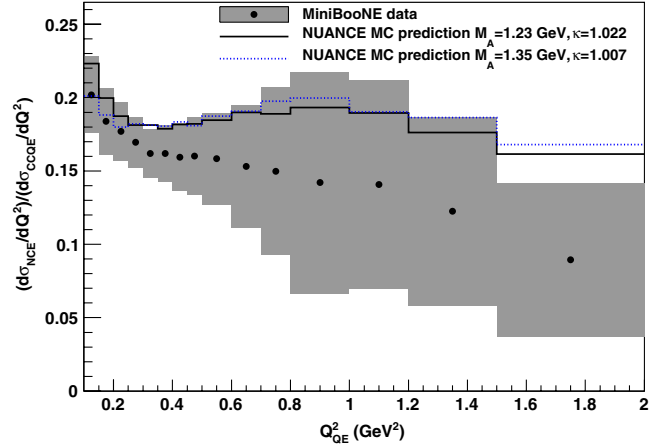Given that MiniBooNE measures a CCQE differential cross section [26] that is ∼30% higher than naive expec-

tations from the relativistic Fermi gas model [29], it is interesting to compare those results with our NCE measurement. To facilitate such a comparison and, at the same time, reduce flux uncertainties, we extract the NCE/CCQE ratio as a function of Q^2_{QE}. In the case of CCQE, Q^2_{QE} has been defined from the outgoing muon kinematics only, assuming a stationary neutron target (see Ref. [26] for details). It should be pointed out that a significant difference exists in how these cross sections are measured in MiniBooNE. As explained earlier, the NCE cross section is calculated from the measured total kinetic energy of final
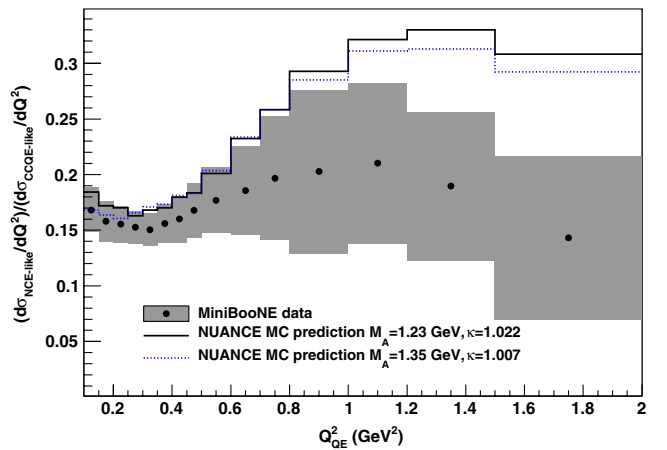

FIG. 7 (color online).   MiniBooNE NCE-like/CCQE-like cross-section ratio on CH_2 as a function of Q^2_{QE} with total error. The color code for the histograms is the same as in Fig. 6.

state nucleons and is mildly sensitive to FSI, whereas the CCQE is calculated entirely from the reconstructed muon and is not sensitive to FSI.

The measured ratio is shown in Fig. 6 together with the NUANCE MC prediction. The data/MC agreement is reasonable within errors.

Adding the MC NCE-like background prediction to the numerator and the MC CCQE-like background prediction to the denominator produces a NCE-like to CCQE-like differential cross-section ratio, which is additionally shown in Fig. 7. This is an even more model-independent measurement, where we do not have to rely on modeling of both NCE-like and CCQE-like backgrounds and claim them as a part of the signal.

The measured NCE/CCQE ratio is consistent with that predicted by the MC. This is an important point when considering possible explanations of the larger than predicted value of the CCQE cross section. The predicted MC ratio is chosen for two values of M_A and κ: One is with $M_A = 1.23$ GeV and $\kappa = 1.022$ as measured in [13], and the second with $M_A = 1.35$ GeV and $\kappa = 1.007$ is from a more recent MiniBooNE CCQE result [26], where κ is a Pauli blocking scaling factor parameter.

There is some disagreement between data and MC for the NCE-like/CCQE-like ratio above $Q^2_{\mathrm{QE}} > 1.0$ GeV^2, but this is where the NCE-like backgrounds (predominantly NC pion channels with pion absorption) become a significant fraction of the signal.

F. Axial vector mass measurement using the NCE cross section

In Appendix B 1 the expression for the NCE differential cross section on free nucleons is described. From there, one can see that the NCE cross section is sensitive to the axial form factor. In fact, at low Q^2, $d\sigma/dQ^2 \sim (F^Z_A)^2(Q^2)$, where

$$F^Z_A(Q^2) = \tfrac{1}{2}(g_A\tau_3 - \Delta s)/(1 + Q^2/M^2_A)^2,$$

where $g_A = 1.2671$ is measured precisely from neutron beta decay [46].

To first order, the MiniBooNE $\nu N \to \nu N$ cross section is not sensitive to Δs, as the linear term in Δs nearly cancels, while the quadratic term in Δs remains but is small if $|\Delta s| \ll g_A$. However, these data are still useful for probing M_A.

A χ^2 goodness of fit test is performed to find the set of M_A and κ parameters, described earlier in Sec. B 2, that best matches data. Varying the values of M_A and κ in the MC model results in different reconstructed NCE energy distributions. For each set of M_A and κ values, a χ^2 is calculated using the full error matrix. The full error matrix in this case also includes an additional uncertainty on Δs of 0.1. The reconstructed energy spectrum for data and MC for different values of M_A and κ (as measured from
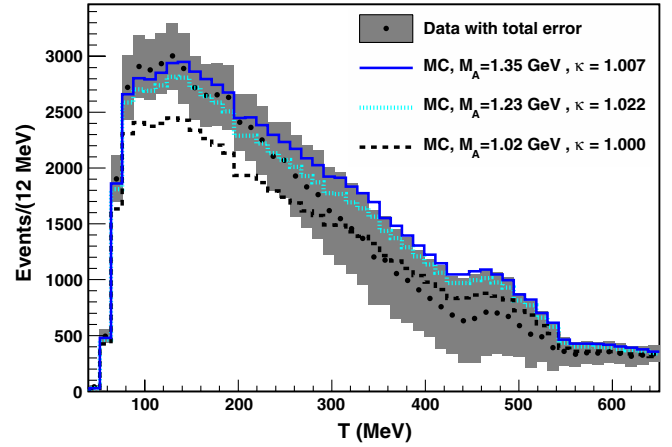

FIG. 8 (color online). χ^2 tests performed on the NCE reconstructed nucleon kinetic energy distribution for MC with different M_A values of 1.35, 1.23, and 1.02 GeV. The χ^2 values are 27.1, 29.2, and 41.3 for 49 degrees of freedom (DOF), respectively. The distributions are normalized to POT.

MiniBooNE CCQE data, as well as the average values prior to MiniBooNE) are shown in Fig. 8. The reconstructed energy distribution of the NCE sample has a negligible sensitivity to κ; however, the higher values of M_A seem to better describe MiniBooNE NCE data.

The NCE data can also be directly fit to independently extract information on M_A and Δs. Because of the quadratic term in Δs in the NCE differential cross-section expression, the shape of χ^2 slightly depends on the value of Δs. Assuming $\Delta s = 0$, the 1σ allowed region of M_A from the MiniBooNE NCE sample yields

$$M_A = 1.39 \pm 0.11 \text{ GeV},$$

with $\chi^2_{\min}/\mathrm{DOF} = 26.9/50$. Using $\Delta s = -0.2$ (which roughly corresponds to the value obtained by the BNL E734 experiment [7]) yields $M_A = 1.35 \pm 0.11$ GeV with $\chi^2_{\min}/\mathrm{DOF} = 24.9/50$. The results from the M_A fit to the NCE data using an absolute (POT) normalization agree well with the shape-only fit results from the MiniBooNE CCQE data [26].

IV. MEASUREMENT OF Δs USING A HIGH ENERGY PROTON-ENRICHED SAMPLE

A. High energy proton-enriched sample

As mentioned above, the Δs sensitivity of the NCE sample comes down to the possibility of distinguishing proton from neutron events. In particular, the ratio of $\nu p \to \nu p$ to $\nu n \to \nu n$ is most sensitive to Δs in addition to reducing the systematic error. One should mention that even though FSI effects may be significant in the NCE cross section, they become negligible when using such ratios [47].

In MiniBooNE, NCE scattering from a neutron can only be detected when that neutron has a further strong

interaction, usually with a proton. At low energies, these cannot be distinguished from NCE scattering from a proton. When scattering kinematics produces a proton above Cherenkov threshold, it is distinctive since the secondary interaction required to detect a neutron rarely produces an above-Cherenkov-threshold proton. We thus select a special class of NCE protons, with only one proton in the final state whose energy is above Cherenkov threshold. These *single proton* events will be used for a Δs measurement.

It should be noted that events with multiple nucleons in the final state (both NCE neutrons and NCE-like background) have *multiple protons* produced in the reaction. At kinetic energies above 350 MeV, single proton events produce on average a higher Cherenkov light fraction than multiple proton events. In addition, these two classes of events differ in the kinematics of the outgoing nucleon, with single proton events being more forward-going.

B. Ratio of $\nu p \rightarrow \nu p$ to $\nu N \rightarrow \nu N$

In order to measure Δs, the ratio of $\nu p \rightarrow \nu p$ to $\nu N \rightarrow \nu N$ as a function of the reconstructed nucleon kinetic energy from 350 to 800 MeV is used. Additionally, by taking the ratio, several sources of systematic uncertainty are reduced. The denominator of this ratio are events with NCE selection cuts described in Sec. III B but with the energy cut (5) replaced with 350 MeV $< T <$ 800 MeV, and an additional "proton/muon" cut based on $\ln(\mathcal{L}_\mu/\mathcal{L}_p)$ (the log-likelihood ratio between muon and proton hypotheses) in order to reduce muonlike backgrounds that dominate the high visible energy region (Fig. 9). After these cuts, the $\nu N \rightarrow \nu N$ data sample includes 24 004 events with the following predicted channel fractions: 45% NCE, 26% NCE-like background, 3% dirt background, and 25% other backgrounds.

FIG. 10 (color online). The proton/neutron cut based on the fraction of prompt hits with the corrected time between 0 and 5 ns. The right part of the cut is used for the analysis. The histograms are normalized to POT.

For the numerator of the ratio, two more cuts are applied in addition to the ones used for the denominator. The first of them, the "proton/neutron" cut, is a variable based on the fraction of prompt light (as described in Sec. III B but with a corrected time between 0 and 5 ns). This cut is to increase the single proton event fraction in the sample. The described variable distribution and the value of the cut are shown in Fig. 10 for both single proton and multiple proton events. As one can see, the cut reduces multiple proton events, which have less Cherenkov light than single proton events. Finally, we apply a cut on the angle between the reconstructed nucleon direction and the incident beam direction. As shown in Fig. 11, single proton events are mostly forward-going; we thus require $\theta_p < 60°$. The final
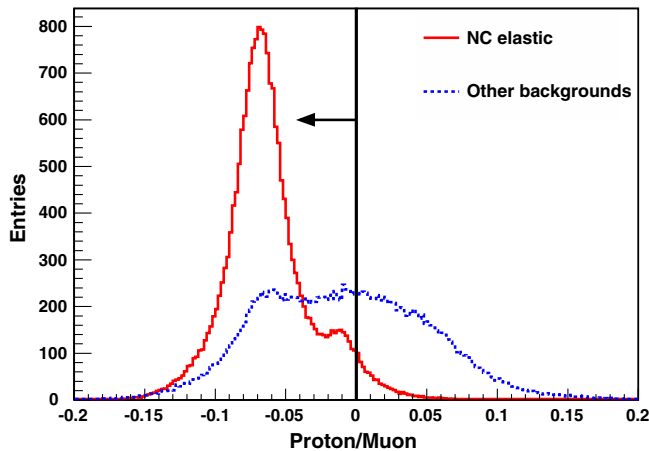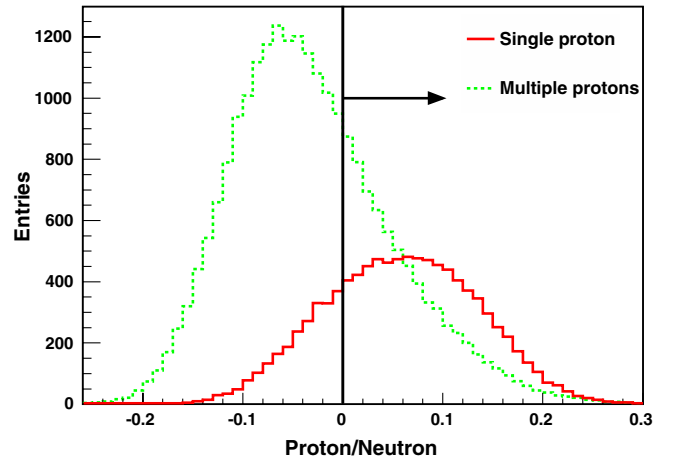

FIG. 9 (color online). The proton/muon cut based on the $\ln(\mathcal{L}_\mu/\mathcal{L}_p)$ variable, which is the log-likelihood ratio of muon and proton event hypotheses. The left part of the cut is used for the analysis. The histograms are normalized to POT.
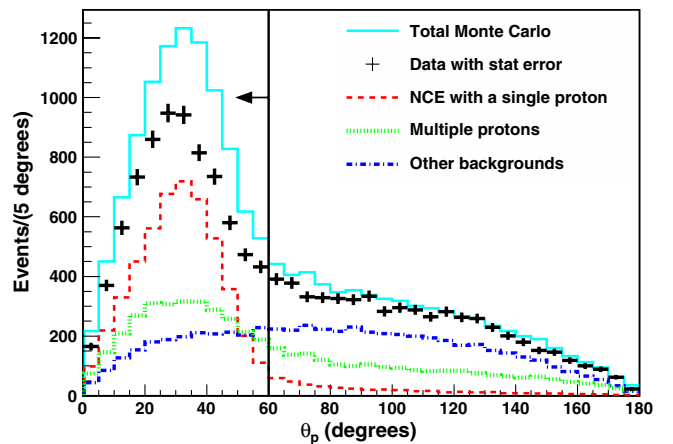

FIG. 11 (color online). The angle between the reconstructed nucleon direction and the incident beam direction for data and MC after the NCE, proton/muon, and proton/neutron cuts. All distributions are POT-normalized. Events with $\theta_p < 60°$ are used in the analysis.
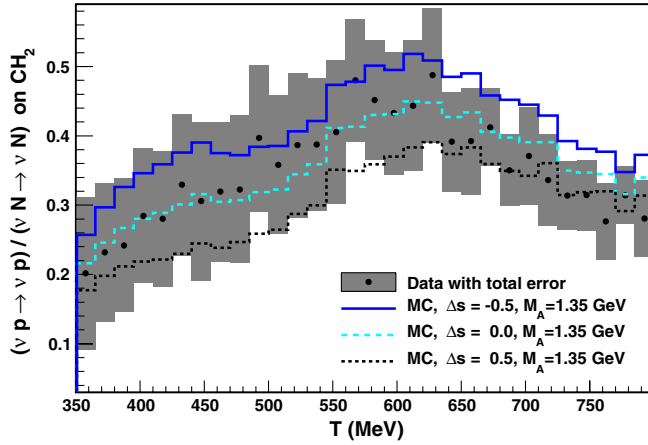
FIG. 12 (color online). The ratio of $\nu p \rightarrow \nu p / \nu N \rightarrow \nu N$ as a function of the reconstructed energy for data and MC with Δs values as labeled.

$\nu p \rightarrow \nu p$ data sample includes 7616 events with the following predicted channel fractions: 55% $\nu p \rightarrow \nu p$, 10% $\nu n \rightarrow \nu n$, 14% NCE-like background, 1% dirt background, and 19% other backgrounds.

The ratio of $\nu p \rightarrow \nu p$ to $\nu N \rightarrow \nu N$ events for data and MC for different values of Δs (-0.5, 0, and $+0.5$) is shown in Fig. 12, which illustrates the sensitivity of this ratio to Δs. The error bars for the data histogram are the diagonal elements of the full error matrix.

C. Measurement of Δs

The full error matrix is used for the χ^2 tests of Δs to determine the best fit and the confidence interval. The χ^2 surface also slightly depends on the value of M_A. Assuming $M_A = 1.35$ GeV, the fit to the MiniBooNE measured $\nu p \rightarrow \nu p / \nu N \rightarrow \nu N$ ratio yields

$$\Delta s = 0.08 \pm 0.26, \qquad (2)$$

with $\chi^2_{\min}/\text{DOF} = 34.7/29$. Using $M_A = 1.23$ GeV yields $\Delta s = 0.00 \pm 0.30$ with $\chi^2_{\min}/\text{DOF} = 34.5/29$. The result is consistent with the BNL E734 measurement [7].

One needs to comment on the implications of Figs. 4, 11, and 12 on the Δs result. From Fig. 4, one can see that the MiniBooNE MC overpredicts the total number of events passing the NCE selection cuts at high reconstructed energies ($T > 250$ MeV) by as much as 40%. The NCE proton-enriched sample was obtained for events with high reconstructed energies $350 < T < 800$ MeV. For these events, looking at the θ_p distribution in Fig. 11, it seems that the entire disagreement between data and MC at these energies comes from the forward-going events, $\nu p \rightarrow \nu p$. Clearly there is a deficit of $\nu p \rightarrow \nu p$ in the data, which in principle implies that this might be due to positive values of Δs. However, Fig. 12 and the result in Eq. (2) shows that it is consistent with zero. This may indicate that there is also a deficit of $\nu n \rightarrow \nu n$.

This measurement represents the first attempt at a Δs determination using this ratio. The systematic errors are quite large, mostly due to large uncertainties in the optical model of the mineral oil. MiniBooNE maintains a sensitivity to Δs for proton energies above Cherenkov threshold for protons, where the contribution from NCE-like background is significant. In order to improve the sensitivity to Δs, future experiments need to have good proton/neutron particle identification (possibly through neutron capture tagging) and extend the cross-section measurement down to the $T < 200$ MeV region, where the contribution from NCE-like background becomes negligible and where the extrapolation of the axial form factor to $Q^2 = 0$ becomes less model-dependent.

V. SUMMARY

In summary, MiniBooNE has used a high-statistics sample of NCE interactions to measure the NCE ($\nu N \rightarrow \nu N$) flux-averaged differential cross section, $d\sigma/dQ^2$ on CH_2. Using MiniBooNE CCQE data, a measurement of NCE/CCQE cross-section ratio has also been performed. Using POT-normalized distributions of the reconstructed energy for the NCE sample, χ^2 tests for several M_A and κ values have been performed. The MC with higher values of M_A give a better χ^2 than that with $M_A = 1.02$ GeV. The allowed region for the axial vector mass using just MiniBooNE NCE data was obtained: $M_A = 1.39 \pm 0.11$ GeV. It is in agreement with the shape normalized fits of ν_μ CCQE scattering on neutrons bound in carbon, oxygen, and iron as obtained by recent experiments [14–16,26].

For energies above Cherenkov threshold, a sample of NCE proton-enriched events was obtained, which was used for the measurement of the $\nu p \rightarrow \nu p$ to $\nu N \rightarrow \nu N$ ratio, which in turn is sensitive to Δs. A value of $\Delta s = 0.08 \pm 0.26$ was extracted, in agreement with the results from the BNL E734 experiment [7].

APPENDIX A: DIRT BACKGROUND MEASUREMENT

The fact that dirt and in-tank events have different spatial distributions, such as reconstructed radius R and the reconstructed Z coordinate (which is in the direction of the beam) can be used to determine the dirt energy spectrum. Dirt event vertices are generally reconstructed closer to the edge of the detector than the in-tank events. Also, dirt events are mostly reconstructed in the upstream part of the detector with $Z < 0$, whereas in-tank events have approximately a uniform distribution in this variable. Additionally, we use the fact that dirt and in-tank events have a very different energy spectrum as seen in Fig. 4.

The dirt energy spectrum is measured by fitting the MC in-tank and dirt templates to the data in Z, R, and energy distributions for the dirt-enriched event samples. The R and Z distributions are obviously correlated. However, the

TABLE II.   Event sample cuts, their respective purposes, and dirt events fractions. The dirt fractions are calculated from the initial MC simulation (before dirt fits), and NCE is the signal sample (cuts from 1 to 7), whereas the other three samples are the dirt-enriched samples for use in the dirt fits.

Sample name	Purpose of the sample	Cuts : Precuts+	Dirt fraction (%)
NCE	NCE sample (dirt-reduced)	$R_{\text{fiducial}}(T)$ [cut (7) in Sec. III B]	13.4
Dirt-Z	Fit dirt from Z (dirt-enhanced)	3.8 m $< R <$ 5.2 m	27.8
Dirt-R	Fit dirt from R (dirt-enhanced)	$Z < 0$ m	34.3
Dirt-E	Fit dirt from energy (dirt-enhanced)	3.8 m $< R <$ 5.2 m and $Z < 0$ m	37.6

samples used for the Z and R fits of the dirt have a large fraction of events that are present in one sample and not in the other.

To measure the dirt background in the NCE event sample, three additional dirt-enriched samples of events are used. For each of the variables (reconstructed Z, R, and energy) different samples are used, based on cutting on the other of these variables; for example, if measuring dirt events from the Z distribution, one would have an additional cut on R.

The samples that are selected for these fits are defined in Table II. The following precuts are the same for each event sample [cuts from (1)–(6) described in Sec. III B]:

$$\text{precuts} = 1 \text{ subevent} + V \text{ hits} < 6 + T \text{ hits} > 24$$
$$+ 4400 \text{ ns} < \text{time} < 6500 \text{ ns} + T$$
$$< 650 \text{ MeV} + \ln(\mathcal{L}_e/\mathcal{L}_p) < 0.42.$$

These are the same as the NCE analysis cuts with the removal of the radial cut. The dirt fraction in the
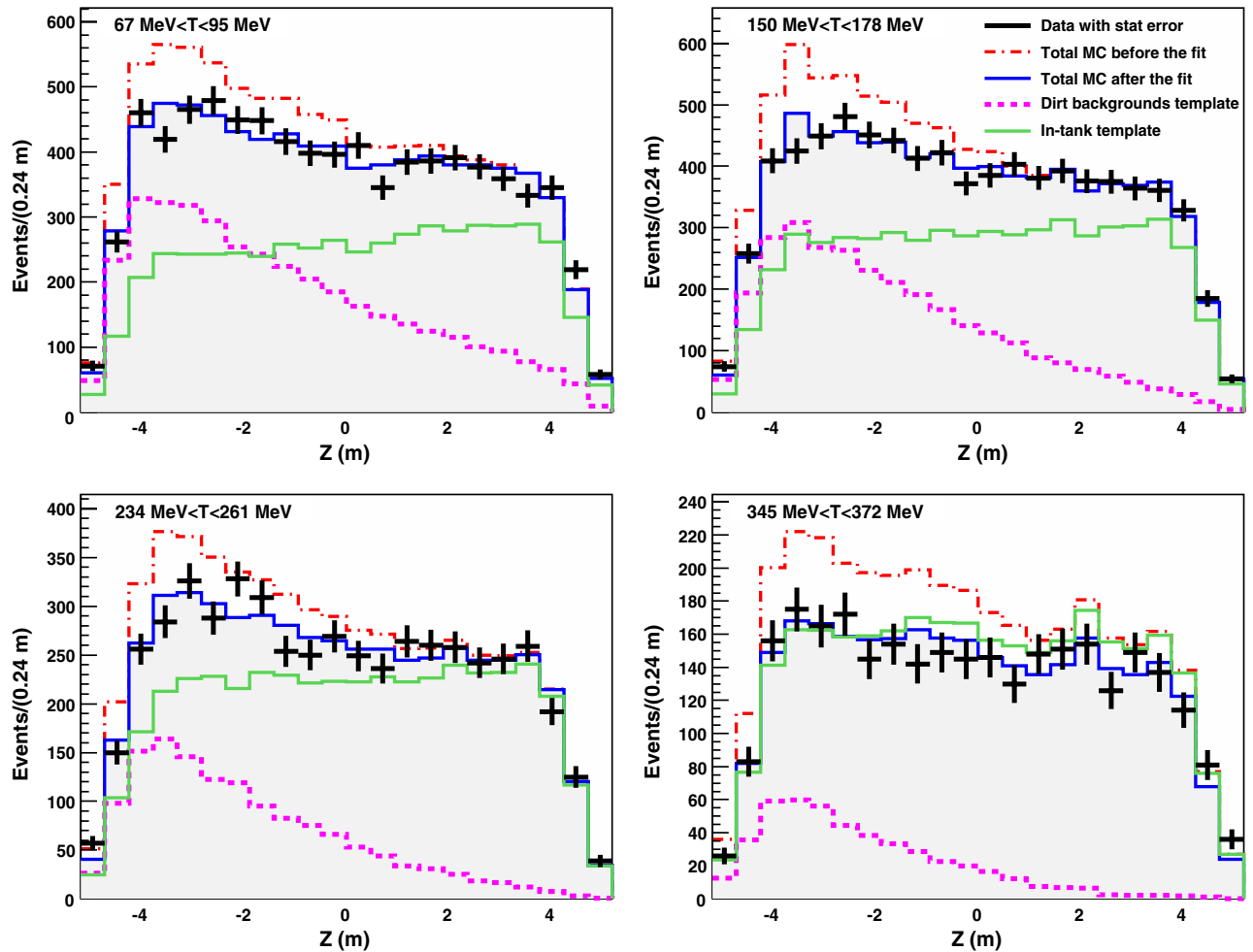

FIG. 13 (color online).   Fits to the data using MC templates for the in-tank and dirt events in Z for different reconstructed energy bins. The "total MC before the fit" is a sum of the in-tank and dirt templates, which are absolutely (POT) normalized.

dirt-enhanced samples is increased significantly, by a factor of 2–3 over the unenhanced sample.

1. Dirt rate measurement from the reconstructed *Z* distribution

To measure the dirt background from the *Z* distribution, the "dirt-*Z*" event sample from Table II is used. The shapes (templates) of the *Z* distribution for the in-tank and dirt events in the MC are used to fit the shape of the *Z* distribution for the data. These fits are done in bins of reconstructed energy *T*, so that in the end one obtains the measured dirt background energy spectrum. From the fits the correction function

$$\text{Corr}_i^{\text{dirt}} = (\text{data}_i/\text{MC}_i)^{\text{dirt}}$$

that should be applied to the MC spectrum of the dirt events is extracted, which is the ratio of the measured to predicted number of dirt events in the *i*th bin.

An example of the fit is shown in Fig. 13 for several intervals of the reconstructed energy. The agreement between the data and MC is much better after the fit.

2. Dirt rate measurement from the reconstructed *R* distribution

This procedure is essentially the same as for the dirt measurement using the *Z* distribution, but instead, the "dirt-*R*" sample from Table II is used and the fitting is done for the *R* variable. Again, from the fits, the correction function for the dirt energy spectrum Corr$^{\text{Dirt}}$ is extracted.

3. Dirt rate measurement from the reconstructed energy distribution

For this method, two event samples are used, the signal (NCE) and the dirt-enriched sample with the "dirt-*E*" cuts from Table II. For both samples, we look at both the MiniBooNE data and the MC prediction for NCE, dirt, and in-tank backgrounds.

Assuming that the fractions of signal and dirt events in both samples are stable relative to MC variations, one can measure the spectrum of dirt events in the NCE sample from the data distribution for both of these samples. We define the following histograms:

ν Reconstructed energy spectrum for data
B   Reconstructed energy spectrum for MC in-tank backgrounds
S   Reconstructed energy spectrum for MC NCE
D   Reconstructed energy spectrum for MC dirt,

which have upper indices describing the event sample, namely,

s   NCE event sample
d   Dirt-*E* event sample.

The new spectra for the dirt and signal events can be determined from fitting the data in both NCE and dirt-*E*

samples. In terms of the definitions that we have introduced, the condition that these spectra coincide in both event samples can be written as

$$B_i^s + S_i^s + D_i^s = \nu_i^s, \qquad B_i^d + S_i^d + D_i^d = \nu_i^d.$$

For each reconstructed energy bin *i* there are 6 unknowns on the left-hand side and 2 knowns on the right-hand side (the data in both NCE and dirt-*E* samples). Assuming a reliable in-tank background prediction, one can fix B_i^s and B_i^d. Then, we introduce the fractions of signal and dirt events in the two samples:

$$f_i = \frac{D_i^d}{D_i^s} \quad \text{and} \quad g_i = \frac{S_i^d}{S_i^s}.$$

Because these variables are ratios, they are relatively stable to MC variations and independent of the dirt and NCE events energy spectra. The functions *f* and *g* are determined from the MC.

Herewith, one can express D_i^s (the dirt energy spectrum in the NCE sample) in terms of the above definitions as

$$D_i^s = \frac{g_i(\nu_i^s - B_i^s) - (\nu_i^d - B_i^d)}{g_i - f_i},$$

which is the measured spectrum of dirt events in the NCE event sample.

Finally, using all three methods, the combined dirt energy spectrum correction function fit is performed. The chosen form of the fit function is linear below 300 MeV and a constant above, as shown in Fig. 14. All of these measurements agree with each other within 10%, lending confidence to our overall ability to constrain the dirt background in the analysis.
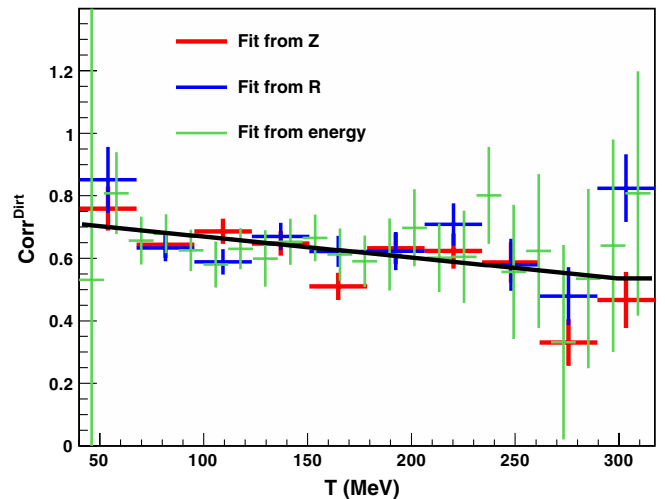

FIG. 14 (color online). Combined dirt energy correction fit from *Z*, *R*, and energy distributions. Errors for *Z* and *R* are statistical from the minimization fitting these distributions. The error for the energy distribution is the largest systematic uncertainty resulting from the optical model of the mineral oil.

The new, measured reconstructed energy spectrum for the dirt events in the NCE sample is calculated as a bin-by-bin correction of the initial MC dirt energy spectrum multiplied by the measured correction function. The measured number of dirt events is determined to be ∼30% lower than the original MC prediction.

APPENDIX B: MINIBOONE NEUTRAL-CURRENT ELASTIC CROSS-SECTION DESCRIPTION

1. Phenomenology

While MiniBooNE uses the relativistic Fermi gas model of Smith and Moniz to describe NCE scattering, it is illustrative to write down the expression for the NCE cross section in the case of a free nucleon target.

The neutrino-nucleon NCE differential cross section on free nucleons can be written as [20]

$$\frac{d\sigma}{dQ^2} = \frac{G_F^2 Q^2}{2\pi E_\nu^2}(A(Q^2) \pm B(Q^2)W + C(Q^2)W^2), \quad \text{(B1)}$$

where the $+$ sign corresponds to neutrinos and the $-$ sign to antineutrinos, $W = 4E_\nu/M_N - Q^2/M_N^2$, and $A(Q^2)$, $B(Q^2)$, and $C(Q^2)$ are form factors defined, respectively, as

$$A(Q^2) = \tfrac{1}{4}[(F_A^Z)^2(1 + \tau) - ((F_1^Z)^2 - \tau(F_2^Z)^2)(1 - \tau)$$
$$+ 4\tau F_1^Z F_2^Z],$$
$$B(Q^2) = \tfrac{1}{4}F_A^Z(F_1^Z + F_2^Z),$$
$$C(Q^2) = \frac{M_N^2}{16Q^2}[(F_A^Z)^2 + (F_1^Z)^2 + \tau(F_2^Z)^2].$$

Here F_1^Z, F_2^Z, and F_A^Z are nucleon Dirac, Pauli, and axial weak neutral-current form factors, respectively, which in general are real dimensionless functions of Q^2, and $\tau = Q^2/4M_N^2$. Each of the nucleon form factors is different for proton and neutron targets. At low Q^2 the $C(Q^2)$ term in Eq. (B1) dominates (see Ref. [43]). Thus, the NCE cross section has a significant contribution from axial vector currents.

Under the conserved vector current [48], one can express the weak form factors through their electromagnetic equivalents:

$$F_i^Z = (\tfrac{1}{2} - \sin^2\theta_W)[F_i^{\mathrm{EM},p} - F_i^{\mathrm{EM},n}]\tau_3$$
$$- \sin^2\theta_W[F_i^{\mathrm{EM},p} + F_i^{\mathrm{EM},n}] - \tfrac{1}{2}F_i^s, \quad i = 1, 2, \quad \text{(B2)}$$

where θ_W is the weak mixing angle, τ_3 is a factor $+1$ for protons and -1 for neutrons, F_i^s are the isoscalar form factors discussed later, and the Dirac and Pauli electromagnetic form factors are

$$F_1^{\mathrm{EM}}(Q^2) = \frac{G_E(Q^2) + \frac{Q^2}{4M_N^2}G_M(Q^2)}{1 + \frac{Q^2}{4M_N^2}},$$

$$F_2^{\mathrm{EM}}(Q^2) = \frac{G_M(Q^2) - G_E(Q^2)}{1 + \frac{Q^2}{4M_N^2}},$$

where G_E and G_M are Sachs form factors [49]. Instead of the dipole approximation the Bodek-Budd-Arrington-2003 form of the Sachs form factors [50] is used in this analysis, which better describes the electron-proton scattering data.

The axial weak form factor by definition can be expressed through its isovector and isoscalar parts:

$$F_A^Z = \frac{\tau_3}{2}F_A - \frac{1}{2}F_A^s. \quad \text{(B3)}$$

The isovector axial form factor can be measured via weak charged current. Usually it is assumed to have a dipole form:

$$F_A(Q^2) = \frac{g_A}{(1 + \frac{Q^2}{M_A^2})^2}, \quad \text{(B4)}$$

where $g_A = F_A(0) = 1.2671$ [46] is measured precisely from neutron beta decay.

The isoscalar form factors F_1^s and F_2^s in Eq. (B2) are usually thought to be due to contributions from strange quarks to the electric charge and to the magnetic moment of the nucleon, whereas F_A^s in Eq. (B3) is their contribution to the nucleon spin. The F_A^s value at $Q^2 = 0$ is called Δs. F_1^s and F_2^s can be extracted from parity-violating electron-scattering experiments. Recent results from the HAPPEX experiment [51] show that these electric and magnetic strange form factors are consistent with zero. The exact expression for the axial isoscalar form factor is unknown, but in analogy to the isovector axial form factor it is usually represented in the dipole form with the same value of the
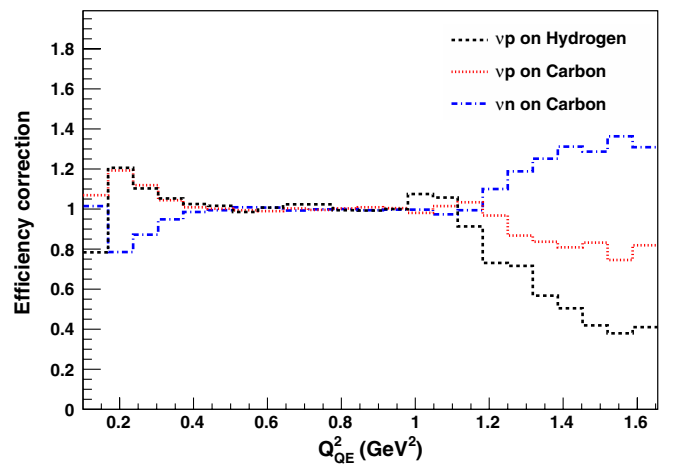

FIG. 15 (color online). Efficiency corrections $C_{\nu p,H}$, $C_{\nu p,C}$, and $C_{\nu n,C}$ versus Q^2_{QE} for different NCE processes (as labeled).

TABLE III.   NCE/CCQE and NCE-like/CCQE-like differential cross-section ratios as a function of $Q^2_{\mathrm{QE}} = 2m_N\sum_i T_i$.

Q^2_{QE}(GeV^2)\distribution	$\frac{\sigma_{\mathrm{NCE}}}{\sigma_{\mathrm{CCQE}}}$	$\frac{\sigma_{\mathrm{NCE-like}}}{\sigma_{\mathrm{CCQE-like}}}$
0.100–0.150	$(2.019 \pm 0.261) \times 10^{-1}$	$(1.682 \pm 0.199) \times 10^{-1}$
0.150–0.200	$(1.839 \pm 0.225) \times 10^{-1}$	$(1.582 \pm 0.181) \times 10^{-1}$
0.200–0.250	$(1.769 \pm 0.199) \times 10^{-1}$	$(1.554 \pm 0.165) \times 10^{-1}$
0.250–0.300	$(1.696 \pm 0.173) \times 10^{-1}$	$(1.526 \pm 0.147) \times 10^{-1}$
0.300–0.350	$(1.619 \pm 0.167) \times 10^{-1}$	$(1.502 \pm 0.145) \times 10^{-1}$
0.350–0.400	$(1.620 \pm 0.192) \times 10^{-1}$	$(1.561 \pm 0.172) \times 10^{-1}$
0.400–0.450	$(1.594 \pm 0.231) \times 10^{-1}$	$(1.601 \pm 0.210) \times 10^{-1}$
0.450–0.500	$(1.602 \pm 0.264) \times 10^{-1}$	$(1.680 \pm 0.244) \times 10^{-1}$
0.500–0.600	$(1.584 \pm 0.313) \times 10^{-1}$	$(1.767 \pm 0.295) \times 10^{-1}$
0.600–0.700	$(1.532 \pm 0.416) \times 10^{-1}$	$(1.855 \pm 0.397) \times 10^{-1}$
0.700–0.800	$(1.498 \pm 0.572) \times 10^{-1}$	$(1.966 \pm 0.554) \times 10^{-1}$
0.800–1.000	$(1.421 \pm 0.755) \times 10^{-1}$	$(2.028 \pm 0.737) \times 10^{-1}$
1.000–1.200	$(1.408 \pm 0.712) \times 10^{-1}$	$(2.102 \pm 0.720) \times 10^{-1}$
1.200–1.500	$(1.226 \pm 0.643) \times 10^{-1}$	$(1.897 \pm 0.666) \times 10^{-1}$
1.500–2.000	$(8.948 \pm 5.248) \times 10^{-2}$	$(1.431 \pm 0.736) \times 10^{-1}$

axial vector mass to minimize the number of free parameters in the model [19]:

$$F^s_A(Q^2) = \frac{\Delta s}{(1+\frac{Q^2}{M_A^2})^2}. \qquad (B5)$$

2. MiniBooNE neutral-current elastic cross-section discussion

The MiniBooNE NCE scattering sample consists of three different processes: scattering on free protons in hydrogen, bound protons in carbon, and bound neutrons in carbon. Because several final state nucleons may be

TABLE IV.   MiniBooNE measured NCE differential cross section, predicted NCE-like background, and predicted correction coefficients for the three different NCE scattering contributions as a function of $Q^2_{\mathrm{QE}} = 2m_N\sum_i T_i$.

Q^2_{QE}(GeV^2)\distribution	NCE cross section, cm^2/GeV^2	NCE-like background, cm^2/GeV^2	$C_{\nu p,H}$	$C_{\nu p,C}$	$C_{\nu n,C}$
0.101–0.169	$(3.361 \pm 0.360) \times 10^{-39}$	4.875×10^{-41}	0.784	1.068	1.014
0.169–0.236	$(2.951 \pm 0.394) \times 10^{-39}$	4.623×10^{-41}	1.206	1.192	0.785
0.236–0.304	$(2.494 \pm 0.429) \times 10^{-39}$	5.879×10^{-41}	1.102	1.119	0.871
0.304–0.372	$(2.089 \pm 0.340) \times 10^{-39}$	8.425×10^{-41}	1.053	1.043	0.949
0.372–0.439	$(1.744 \pm 0.243) \times 10^{-39}$	1.235×10^{-40}	1.024	1.009	0.985
0.439–0.507	$(1.432 \pm 0.246) \times 10^{-39}$	1.647×10^{-40}	1.016	1.002	0.994
0.507–0.574	$(1.168 \pm 0.260) \times 10^{-39}$	1.964×10^{-40}	0.986	0.994	1.009
0.574–0.642	$(9.435 \pm 2.400) \times 10^{-40}$	2.155×10^{-40}	1.007	0.989	1.008
0.642–0.709	$(7.534 \pm 2.205) \times 10^{-40}$	2.222×10^{-40}	1.023	1.002	0.992
0.709–0.777	$(6.015 \pm 2.194) \times 10^{-40}$	2.215×10^{-40}	1.023	0.995	0.998
0.777–0.844	$(4.832 \pm 2.320) \times 10^{-40}$	2.075×10^{-40}	0.994	1.003	0.999
0.844–0.912	$(3.854 \pm 2.331) \times 10^{-40}$	1.890×10^{-40}	0.993	1.009	0.994
0.912–0.980	$(3.209 \pm 2.330) \times 10^{-40}$	1.756×10^{-40}	0.999	1.004	0.997
0.980–1.047	$(2.649 \pm 2.117) \times 10^{-40}$	1.521×10^{-40}	1.074	0.980	0.997
1.047–1.115	$(2.226 \pm 1.818) \times 10^{-40}$	1.265×10^{-40}	1.056	1.015	0.973
1.115–1.182	$(1.935 \pm 1.295) \times 10^{-40}$	1.081×10^{-40}	0.913	1.034	0.994
1.182–1.250	$(1.598 \pm 0.939) \times 10^{-40}$	9.324×10^{-41}	0.731	0.967	1.099
1.250–1.317	$(1.329 \pm 0.769) \times 10^{-40}$	8.079×10^{-41}	0.716	0.867	1.187
1.317–1.385	$(1.111 \pm 0.689) \times 10^{-40}$	6.983×10^{-41}	0.567	0.836	1.251
1.385–1.452	$(9.259 \pm 6.254) \times 10^{-41}$	5.958×10^{-41}	0.504	0.808	1.312
1.452–1.520	$(7.975 \pm 5.373) \times 10^{-41}$	5.229×10^{-41}	0.419	0.832	1.286
1.520–1.588	$(6.618 \pm 4.524) \times 10^{-41}$	4.342×10^{-41}	0.378	0.746	1.363
1.588–1.655	$(5.799 \pm 3.921) \times 10^{-41}$	3.839×10^{-41}	0.410	0.818	1.309

produced, we define the interaction in carbon using the most energetic final state nucleon. This means, for example, that it is possible for an event to be tagged as a NCE neutron, because it has a neutron as the most energetic final state nucleon, even though the original neutrino interaction was on a proton. According to NUANCE, the probability of this misidentification grows almost linearly from about 8% at $Q^2_{QE} = 0.1$ GeV^2 to 16% at $Q^2_{QE} = 1.6$ GeV^2.

The result shown in Fig. 5 is the flux-averaged NCE differential cross section on CH$_2$, averaged over these processes. Herewith, the $\nu N \rightarrow \nu N$ cross section is expressed as

$$\frac{d\sigma_{\nu N \rightarrow \nu N}}{dQ^2} = \frac{1}{7} C_{\nu p,H}(Q^2_{QE}) \frac{d\sigma_{\nu p \rightarrow \nu p,H}}{dQ^2} + \frac{3}{7} C_{\nu p,C}(Q^2_{QE})$$
$$\times \frac{d\sigma_{\nu p \rightarrow \nu p,C}}{dQ^2} + \frac{3}{7} C_{\nu n,C}(Q^2_{QE}) \frac{d\sigma_{\nu n \rightarrow \nu n,C}}{dQ^2},$$
(B6)

where $d\sigma_{\nu p \rightarrow \nu p,H}/dQ^2$ is the NCE cross section on free protons (per free proton), $d\sigma_{\nu p \rightarrow \nu p,C}/dQ^2$ is the NCE cross section on bound protons (per bound proton), and $d\sigma_{\nu n \rightarrow \nu n,C}/dQ^2$ is the NCE cross section on bound neutrons (per bound neutron). The efficiency correction functions $C_{\nu p,H}$, $C_{\nu p,C}$, and $C_{\nu n,C}$ result from different selection efficiencies for each type of NCE scattering process and are estimated from the MC as functions of Q^2_{QE}—as shown in Fig. 15. They are defined as the ratios of the efficiency for a particular type of NCE event to the average efficiency for all NCE events in bins of Q^2_{QE}.

As one can see from Fig. 15, the efficiency correction functions are equal to unity in the region of Q^2_{QE} from 0.4 to 1.2 GeV^2. However, at higher Q^2_{QE}, NCE neutrons have higher efficiency, thus having a higher probability than NCE protons to pass the $T < 650$ MeV cut used in the selection. Similarly, at lower Q^2_{QE}, NCE neutrons have lower probability than NCE protons to pass a T hits > 24 cut.

To calculate a cross section which is to be compared to the MiniBooNE results (as in Fig. 5), one needs to apply these efficiency corrections to each predicted distribution. However, note that in the bulk of the measured region $0.1 < Q^2_{QE} < 1.0$ GeV^2, they are all roughly equivalent to unity.

Finally, we present tables with the NCE/CCQE differential cross-section ratios in Table III and the NCE differential cross section, NCE-like background, and correction coefficients in Table IV. There is also an alternative method of reporting the results of this analysis, namely, in terms of the reconstructed nucleon kinetic energy. The tables for the latter can be found in [43,52]. In order to make use of these results, one would have to follow the instructions described in Appendix B of Ref. [43].

---

[1] D. Cline *et al.*, Phys. Rev. Lett. **37**, 252 (1976).
[2] M. Pohl *et al.*, Phys. Lett. **72B**, 489 (1978).
[3] H. Faissner *et al.*, Phys. Rev. D **21**, 555 (1980).
[4] P. Coteus, M. Diesburg, R. Fine, W. Lee, P. Sokolsky, R. Brown, S. Fuess, P. Nienaber, T. O'Halloran, and Y. Y. Lee, Phys. Rev. D **24**, 1420 (1981).
[5] A. Entenberg *et al.*, Phys. Rev. Lett. **42**, 1198 (1979).
[6] J. Horstkotte *et al.*, Phys. Rev. D **25**, 2743 (1982).
[7] L. A. Ahrens *et al.*, Phys. Rev. D **35**, 785 (1987).
[8] L. A. Ahrens *et al.*, Phys. Rev. D **34**, 75 (1986).
[9] A. A. Aguilar-Arevalo *et al.* (MiniBooNE Collaboration), Phys. Rev. D **79**, 072002 (2009).
[10] A. A. Aguilar-Arevalo *et al.* (MiniBooNE Collaboration), Nucl. Instrum. Methods Phys. Res., Sect. A **599**, 28 (2009).
[11] D. C. Cox, FERMILAB-THESIS-2008-08.
[12] V. Bernard, L. Elouadrhiri, and U. G. Meissner, J. Phys. G **28**, R1 (2002).
[13] A. A. Aguilar-Arevalo *et al.* (MiniBooNE Collaboration), Phys. Rev. Lett. **100**, 032301 (2008).
[14] R. Gran *et al.* (K2K Collaboration), Phys. Rev. D **74**, 052002 (2006).
[15] X. Espinal and F. Sanchez (K2K Collaboration), AIP Conf. Proc. **967**, 117 (2007).
[16] M. E. Dorman, FERMILAB-THESIS-2008-72.
[17] M. Martini, M. Ericson, G. Chanfray, and J. Marteau, Phys. Rev. C **80**, 065501 (2009).
[18] O. Benhar, P. Coletti, and D. Meloni, Phys. Rev. Lett. **105**, 132301 (2010).
[19] G. T. Garvey, W. C. Louis, and D. H. White, Phys. Rev. C **48**, 761 (1993).
[20] G. Garvey, E. Kolbe, K. Langanke, and S. Krewald, Phys. Rev. C **48**, 1919 (1993).
[21] W. M. Alberico *et al.*, Nucl. Phys. **A651**, 277 (1999).
[22] L. Bugel *et al.* (FINeSSE Collaboration), arXiv:hep-ex/0402007.
[23] S. Agostinelli *et al.* (GEANT4 Collaboration), Nucl. Instrum. Methods Phys. Res., Sect. A **506**, 250 (2003).
[24] M. Catanesi *et al.* (HARP Collaboration), Eur. Phys. J. C **52**, 29 (2007).
[25] "Miniboone Flux Data Release," http://www-boone.fnal.gov/for_physicists/data_release/flux.
[26] A. A. Aguilar-Arevalo *et al.* (MiniBooNE Collaboration), Phys. Rev. D **81**, 092005 (2010).
[27] S. J. Brice *et al.*, Nucl. Instrum. Methods Phys. Res., Sect. A **562**, 97 (2006).
[28] D. Casper, Nucl. Phys. B, Proc. Suppl. **112**, 161 (2002).

[29] R. A. Smith and E. J. Moniz, Nucl. Phys. **B43**, 605 (1972); **B101**, 547(E) (1975).

[30] D. Rein and L. M. Sehgal, Nucl. Phys. **B223**, 29 (1983).

[31] G. M. Radecky *et al.*, Phys. Rev. D **25**, 1161 (1982).

[32] J. Campbell *et al.*, Phys. Rev. Lett. **30**, 335 (1973).

[33] S. J. Barish *et al.*, Phys. Rev. D **19**, 2521 (1979).

[34] T. Kitagaki *et al.*, Phys. Rev. D **34**, 2554 (1986).

[35] G. P. Zeller, in *Proceedings of the Third International Workshop on NO-VE: Neutrino Oscillations in Venice: 50 Years after the Neutrino Experimental Discovery, Venice, Italy, 2006*, edited by Milla Baldo Ceolin (Edizioni Papergraf, Padua, 2006).

[36] D. Ashery, I. Navon, G. Azuelos, H. K. Walter, H. J. Pfeiffer, and F. W. Schlepütz, Phys. Rev. C **23**, 2173 (1981).

[37] M. K. Jones, R. D. Ransome, V. R. Cupps, R. W. Fergerson, C. L. Morris, J. A. McGill, J. D. Zumbro, J. R. Comfort, B. G. Ritchie, J. R. Tinsley, P. C. Gugelot, and C. F. Moore, Phys. Rev. C **48**, 2800 (1993).

[38] R. D. Ransome, C. L. Morris, M. K. Jones, B. G. Ritchie, D. L. Watson, J. A. McGill, K. Pujara, D. B. Clayton, I. Brown, P. Campbell, and C. F. Moore, Phys. Rev. C **46**, 273 (1992).

[39] R. Brun *et al.*, CERN-DD/EE/84-1, 1987.

[40] C. Zeitnitz and T. A. Gabriel, Nucl. Instrum. Methods Phys. Res., Sect. A **349**, 106 (1994).

[41] A. Fasso *et al.*, in Proceedings of the Workshop on Simulating Accelerator Radiation Environments, Santa Fe, 1993 (unpublished).

[42] K. B. M. Mahn, FERMILAB-THESIS-2009-22.

[43] D. Perevalov, FERMILAB-THESIS-2009-47.

[44] H. Takei, FERMILAB-THESIS-2009-19.

[45] G. D'Agostini, Nucl. Instrum. Methods Phys. Res., Sect. A **362**, 487 (1995).

[46] C. Amsler *et al.* (Particle Data Group), Phys. Lett. B **667**, 1 (2008).

[47] A. Meucci, C. Giusti, and F. D. Pacati, Nucl. Phys. **A773**, 250 (2006).

[48] E. Pachos, *Electroweak Theory* (Cambridge University Press, Cambridge, England, 2007).

[49] F. J. Ernst, R. G. Sachs, and K. C. Wali, Phys. Rev. **119**, 1105 (1960).

[50] H. Budd, A. Bodek, and J. Arrington, arXiv:hepex/0308005.

[51] A. Acha *et al.* (HAPPEX Collaboration), Phys. Rev. Lett. **98**, 032301 (2007).

[52] ''Miniboone Neutral Current Elastic Data Release,'' http://www-boone.fnal.gov/for_physicists/data_release/ncel.